Analysis and Control of Critical Conduction Mode High-Frequency Single-Phase Transformerless PV Inverter

Gibong Son, *Student Member, IEEE*, Zhengrong Huang, *Student Member, IEEE*, Qiang Li, *Member, IEEE*, and Fred C. Lee, *Life Fellow, IEEE*

***Abstract*—This article presents a critical conduction mode (CRM) single-phase transformerless full-bridge inverter in a residential photovoltaic system. The CRM full-bridge inverter in bipolar mode features zero-voltage switching capability for the whole line cycle. This enables the inverter to push switching frequency up to hundreds of kHz and achieve high power density with high efficiency. However, CRM operation incurs nonconstant common mode (CM) voltage during the resonant period, causing high frequency leakage current. To minimize the leakage current, a new switching modulation strategy is proposed introducing triangular current mode (TCM) near the ac voltage zero crossing. The switching modulation scheme alleviates the CM voltage by shortening the resonant period and consequently reduces the leakage current. Then, discontinuous conduction mode is inserted between the CRM and TCM operation regions to improve light load efficiency. In this article, the basic operation principle of the CRM full-bridge inverter, impacts of CRM operation on the leakage current, and details of the proposed switching modulation method are discussed. Experimental results with a 2.4-kW prototype built with GaN devices validate its performance.**

***Index Terms*—Critical conduction mode (CRM), leakage current, soft-switching, single phase transformerless PV inverter, triangular current mode(TCM), zero-voltage switching.**

I. INTRODUCTION

IN RESIDENTIAL photovoltaic (PV) systems, and particularly those considered to be 2 to 8 kW power level, single-phase transformerless inverters have been widely used [1]–[3]. Unlike conventional PV inverters, the transformerless PV inverter does not have a line frequency transformer connecting the inverter to the grid; this enables the PV system to have a simple structure and accomplish high efficiency. Despite the removal of the transformer, products in the market have power density lower than 10 W/in^3 with 97–99% peak efficiency. Since using Si-based power devices limit the switching frequency of the inverter to around 20–30 kHz in order to reduce switching loss, passive components become large, thus impeding high power density. The switching loss of the power devices has been a bottleneck for further improvements in power density and efficiency.

As a result of remarkable developments in wide-bandgap (WBG) devices in the past few years [4]–[7], switching frequency is likely to be pushed to higher levels due to better figure of merit. For example, with a small total gate charge, Q_G, and no reverse recovery charge, Q_{RR}, turn-ON and turn-OFF energy of GaN devices is much smaller than those of Si-based devices. Nevertheless, it is still challenging to push switching frequency up to several hundreds of kHz in continuous conduction mode (CCM) because of high turn-ON loss by hard-switching. Hence, soft-switching turn-ON is essential for higher frequency operation.

Research has been extensively conducted on critical conduction mode (CRM) operation with WBG devices in ac-dc rectifiers and dc-ac inverters running at very high switching frequency [8]–[13]. In CRM, when inductor current reaches zero, the inductor and the output capacitors of the switches resonate. During the resonant period, the drain-to-source voltage of the active switch goes down to zero and zero-voltage switching (ZVS) can be achieved eliminating the turn-ON loss. The fact that the turn-ON energy of a GaN device is dominant and the turn-OFF energy is negligible renders CRM more attractive with the GaN device. Although CRM enlarges the peak and the rms value of the inductor current leading to higher conduction loss and turn-OFF loss, the substantial turn-ON loss reduction makes up for the increased losses. It can be implied from previous works that for residential PV inverters, there is a great chance to enhance power density with high efficiency by operating in CRM with GaN devices.

Incidentally, the leakage current issue needs to be considered in a transformerless PV inverter since a galvanic connection between the grid and PV panel exits. The leakage current flows through the stray capacitance of the PV panel, and that might cause a serious safety problem. Based on an international

---

Manuscript received October 9, 2020; revised February 23, 2021 and March 31, 2021; accepted May 1, 2021. Date of publication May 6, 2021; date of current version July 30, 2021. This work was supported in part at the Applied Power Electronics Conference (APEC) 2020, New Orleans, LA, USA, March 2020. Recommended for publication by Associate Editor V. Agarwal. *(Corresponding author: Gibong Son.)*

Gibong Son is with the Center for Power Electronics Systems, Virginia Tech, Blacksburg, VA 24061, United States (e-mail: gbson@vt.edu).

Zhengrong Huang is with the Analog Devices Inc., Santa Clara, CA USA (e-mail: zrhuang7@vt.edu).

Qiang Li is with the Center for Power Electronics Systems, Virginia Tech, Blacksburg, VA 24061-0131, United States (e-mail: lqvt@vt.edu).

Fred C. Lee is with the ECE, Virginia Tech, Blacksburg, VA 24061-0131, United States (e-mail: fclee@vt.edu).

Color versions of one or more figures in this article are available at https://doi.org/10.1109/TPEL.2021.3078135.

Digital Object Identifier 10.1109/TPEL.2021.3078135

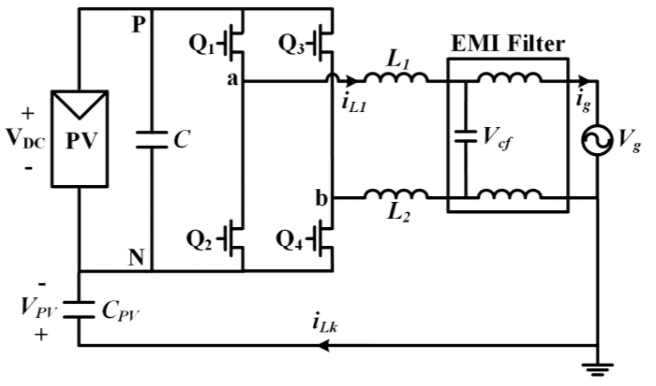

Fig. 1. Single-phase transformerless full-bridge inverter with GaN devices.

standard requirement [14], the rms value of the leakage current needs to be suppressed below 300 mA. In an effort to resolve the issue, a variety of inverter topologies have been introduced. The leakage current can be reduced by cutting the path between the PV panel and the grid at either the dc side [15]–[20] or the ac side [21]–[23]. Making the inverter a perfect symmetrical structure as explained in [24] is also a very effective way to solve the problem. Among the topological approaches, the full-bridge inverter shown in Fig. 1 with bipolar pulse width modulation (PWM) is regarded as the simplest and the most effective topology from the leakage current suppression point of view. In CCM, the common mode (CM) voltage of the inverter, a source of high frequency leakage current, remains constant, resulting in no high frequency leakage current. It is imperative the leakage current is still kept very small in CRM operation; however, analysis of the leakage current in a transformerless PV inverter operating in CRM has not yet been studied.

This article explores a CRM full-bridge inverter with bipolar PWM for a single-phase transformerless PV inverter. Section II explains the power stage operation and inherent ZVS capability of the inverter in detail. In Section III, the leakage current in a transformerless PV inverter is briefly reviewed, as well as an analysis of how CRM operation affects the leakage current. A new switching modulation scheme for leakage current reduction is proposed in Section IV. Moreover, based on the proposed control method, further modified control is introduced to address the tradeoff between efficiency and leakage current. In Section V, experimental results with a laboratory prototype are provided to evaluate the performance of the proposed switching modulation strategies. Lastly, the article is concluded in Section VI.

II. CRITICAL CONDUCTION MODE FULL-BRIDGE INVERTER WITH BIPOLAR PULSE WIDTH MODULATION: OPERATION PRINCIPLES ANALYSIS

The operation modes of a CRM full-bridge inverter with bipolar PWM in one switching cycle at the positive half line cycle are illustrated in Fig. 2. For easier understanding, the EMI filter and the stray capacitance of the PV panel, C_{PV} in Fig. 1, are omitted here. Also, it is assumed that the ac voltage V_g is constant for each switching cycle. During the positive half line cycle, Q_1 and Q_4 act as active switches, and Q_2 and Q_3 act as synchronous rectifiers (SRs). There are two resonant periods as in Fig. 2(b) and (d) when all switches are turned OFF. The second resonance is observed in CRM operation, but not in CCM operation, that is, the key part for achieving ZVS. In Fig. 3(a), gate signals for Q_1–Q_4, L_1 inductor current i_{L1}, and drain-to-source voltage of Q_1 $V_{\text{DS\_Q1}}$ for a switching cycle are depicted. The corresponding state-plane trajectory for $Z_n i_{L1}$ versus $V_{\text{DS\_Q1}}$ are plotted in Fig. 3(b) where Z_n is the characteristic impedance of the inverter during the resonant periods, L is equal to sum of L_1 and L_2, and C_{oss} is the output capacitance of each switch, respectively.

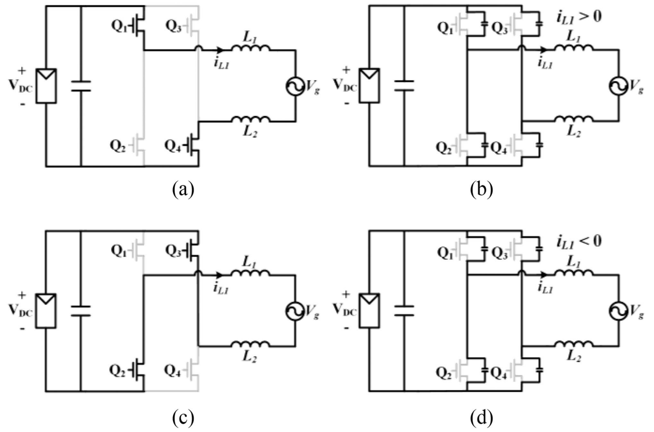

Fig. 2. CRM full-bridge inverter with bipolar PWM operation modes in one switching cycle at the positive half line cycle. (a) Active switches ON. (b) First resonance. (c) SR switches ON. (d) Second resonance.

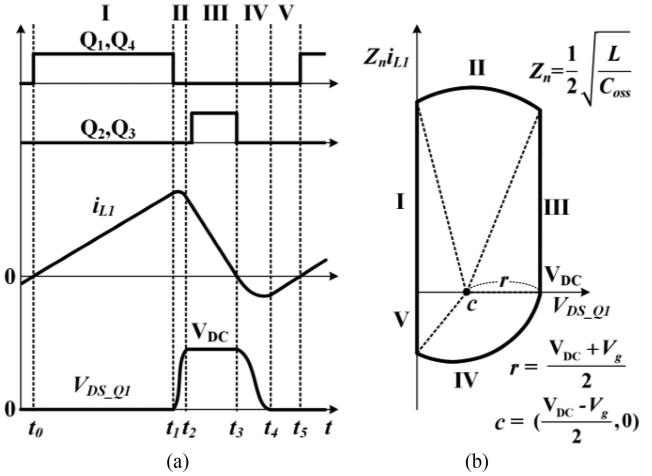

Fig. 3. Switching cycle behavior of CRM full-bridge inverter with bipolar PWM. (a) L_1 inductor current and drain-to-source voltage Q_1 waveforms. (b) State-plane trajectory of L_1 inductor current and drain-to-source voltage of Q_1.

Stage I [t_0–t_1 Interval]: Active switches Q_1 and Q_4 are turned ON as shown in Fig. 2(a). During this period, the inductor current increases. L_1 current and Q_1 drain-to-source voltage are expressed as

$$V_{\text{DS\_Q1}}(t) = 0 \tag{1a}$$

$$i_{L1}(t) = \frac{V_{\text{DC}} - V_g}{L}(t - t_0). \tag{1b}$$

Stage II [t_1–t_2 Interval]: When the active switches Q_1 and Q_4 are turned OFF, the inverter forms the second-order LC circuit as shown in Fig. 2(b) in which the output capacitors of all switches Q_1–Q_4 and inductors L_1 and L_2 participate in the resonance. L_1 and L_2 inductor currents charge the output capacitors of Q_1 and Q_4 and discharge those of Q_2 and Q_3. This period lasts until the drain-to-source voltage of the active switches reaches V_{DC}

$$V_{\mathrm{DS\_}Q1}(t) = \frac{-V_g + V_{\mathrm{DC}}}{2} + \frac{V_g - V_{\mathrm{DC}}}{2}\cos\omega_0(t-t_1) + I_{L1}Z_n\sin\omega_0(t-t_1) \tag{2a}$$

$$i_{L1}(t) = \frac{V_g - V_{\mathrm{DC}}}{2Z_n}\sin\omega_0(t-t_1) + I_{L1}cos\omega_0(t-t_1) \tag{2b}$$

$$\omega_0 = \frac{1}{\sqrt{LC_{oss}}} \tag{2c}$$

where I_{L1} is the initial inductor current value at t_1 instant and ω_0 is the resonant frequency of the circuit. During this period, $V_{\mathrm{DS\_Q1}}$ increases from zero to V_{DC}.

Stage III [t_2–t_3 Interval]: When $V_{\mathrm{DS\_Q1}}$ reaches V_{DC}, the inductor current flows through Q_2 and Q_3 as shown in Fig. 2(c). First, the GaN devices are reversely conducted. Although there is no body diode, the current can flow from source to drain that is one of the notable features of GaN devices. Then, Q_2 and Q_3 are turned ON as SRs to reduce the conduction loss. The turn-ON instant for Q_2 and Q_3 can be anytime between t_2 and t_3, but it is better to be close to t_2. Normally, the turn-ON instant is determined by the required minimum deadtime between active switches and SRs to avoid shoot-through; this is because the required deadtime is longer than the time interval during Stage II. The inductor current decreases, and this period lasts until the inductor current touches zero

$$V_{\mathrm{DS\_}Q1}(t) = V_{\mathrm{DC}} \tag{3a}$$

$$i_{L1}(t) = \frac{-V_{\mathrm{DC}} - V_g}{L}(t-t_2) + I_{L2} \tag{3b}$$

where I_{L2} is the initial inductor current value at t_2 instant.

Stage IV [t_3–t_4 Interval]: When the inductor current touches zero, the SRs are turned OFF. Then, the second resonance begins with the initial condition V_{DC} for $V_{\mathrm{DS\_Q1}}$ and zero for i_{L1}, respectively. The inductor current becomes negative and the drain-to-source voltage of Q_1 starts to decrease and reach zero as follows:

$$V_{\mathrm{DS\_}Q1}(t) = \frac{-V_g + V_{\mathrm{DC}}}{2} + \frac{V_g + V_{\mathrm{DC}}}{2}\cos\omega_0(t-t_3) \tag{4a}$$

$$i_{L1}(t) = -\frac{V_g + V_{\mathrm{DC}}}{2Z_n}\sin\omega_0(t-t_3). \tag{4b}$$

Stage V [t_4–t_5 Interval]: When $V_{\mathrm{DS\_Q1}}$ becomes zero, Q_1 and Q_4 switches are conducted as shown in Fig. 2(a). However, the inductor current direction is different from Stage I and the switches are reversely conducted. Equations for L_1 current and Q_1 drain-to-source voltage are exactly the same as (1) except that Stage V has the initial current. The active switches can be turned ON at any time during Stage V.

By combining the two equations in (4), the following expression for the state-plane trajectory is yielded

$$(Z_n i_{L1})^2 + \left(V_{DS\_Q1} - \frac{V_{\mathrm{DC}} - V_g}{2}\right)^2 = \left(\frac{V_{\mathrm{DC}} + V_g}{2}\right)^2. \tag{5}$$

It can be seen from (5) that the center of the trajectory, $(V_{\mathrm{DC}} - V_g)/2$, is always smaller than the radius of the trajectory during Stage IV, $(V_{\mathrm{DC}} + V_g)/2$. This ensures that the drain-to-source voltage of Q_1 always reaches zero at the end of Stage IV and Q_1 and Q_4 are conducted in the reverse way. Since the active switches are turned ON after t_4, the full-bridge inverter in bipolar mode can attain ZVS intrinsically, irrespective of operating conditions.

III. LEAKAGE CURRENT ANALYSIS IN CRM FULL-BRIDGE INVERTER WITH BIPOLAR PWM

A. *Leakage Current in Transformerless PV Inverter*

In a transformerless PV inverter system, there are two types of leakage currents [25]. One type is line frequency leakage current, $i_{\mathrm{Lk\_}L}$, and the other is high frequency leakage current, $i_{\mathrm{Lk\_}H}$ as illustrated in Fig. 4. The line frequency leakage current is some part of the current coming out from the PV panel. Most of the current goes back into the inverter itself, but a small portion flows through the stray capacitance and becomes the line frequency leakage current. The high frequency leakage current comes out from the switching node of each phase leg, nodes a and b, and goes back into the switching nodes again. It should be mentioned that the single-phase ac system in which the earth ground is

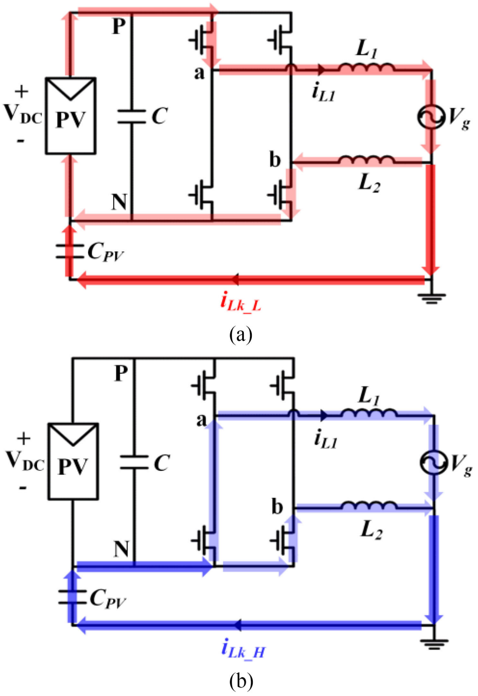

(a)

(b)

Fig. 4. Leakage current path. (a) Line frequency element coming out from the PV panel. (b) High frequency element coming out from switching node of each phase leg.

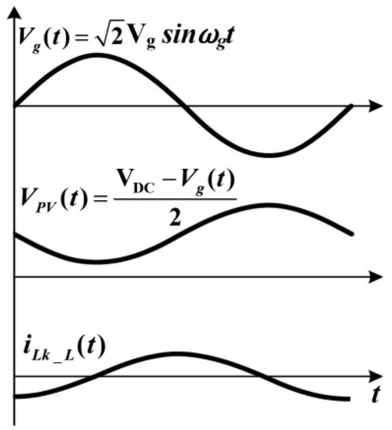

Fig. 5. Line frequency leakage current of transformerless PV inverter.

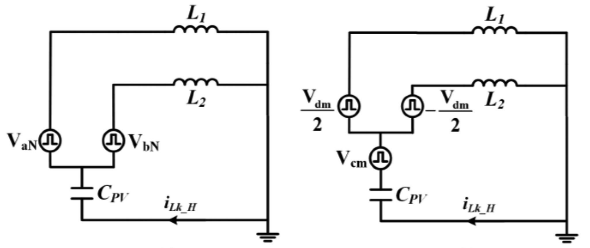

(a) (b)

Fig. 6. Equivalent circuit model for high frequency leakage current. (a) Expressed with switching node voltage V_{aN} and V_{bN}, (b) Expressed with V_{dm} and V_{cm}.

connected to one terminal of the ac voltage is solely taken into account here.

As for the line frequency element shown in Fig. 5, it is generated by the voltage across the stray capacitance, V_{PV}, over the line cycle and presented as

$$i_{\mathrm{Lk}\_L}(t) = C_{\mathrm{PV}}\frac{dV_{\mathrm{PV}}(t)}{dt} = -\omega_g C_{\mathrm{PV}}\sqrt{2}\cos\omega_g t \qquad (6)$$

where ω_g represents the frequency of the ac voltage. The line frequency leakage current is normally small (about tens of mA at most) under wet weather conditions, such as after a rainy day and condensation in the morning. Yet, it is hard to avoid and control the line frequency leakage current, as half of the ac voltage is always excited across C_{PV} [26].

When it comes to the high frequency element [27], the voltage on the switching nodes of the inverter (V_{aN} and V_{bN}) becomes the source of the leakage current illustrated in Fig. 6(a). Again, the EMI filter is left out for a simpler explanation. Also, to consider only the high frequency elements of the circuit, the ac voltage is shorted. In Fig. 6(b), the switching node voltages are separated into CM voltage V_{cm} and differential mode voltage V_{dm} defined as follows:

$$V_{\mathrm{cm}} = \frac{V_{aN} + V_{bN}}{2} \qquad (7a)$$

$$V_{\mathrm{dm}} = V_{aN} - V_{bN}. \qquad (7b)$$

On the assumption that the output inductors L_1 and L_2 are perfectly identical, the two voltage sources including the V_{dm} term can be cancelled out. Then, it has no impact on the high frequency leakage current such that V_{cm} is the only source. Consequently, the equation for the high frequency leakage current in Laplace domain is given by

$$i_{\mathrm{Lk}\_H}(s) = \frac{V_{\mathrm{cm}}}{s(L_1//L_2) + (1/sC_{\mathrm{PV}})}. \qquad (8)$$

It can be inferred from (8) that one can suppress i_{Lk_H} by keeping V_{cm} constant. In other words, no variation in V_{cm} makes it possible to get rid of the high frequency leakage current entirely. To summarize, the line frequency leakage current is very small, but hard to control; however, the high frequency leakage current can be controlled by having constant V_{cm}.

B. Impact of CRM Operation on Leakage Current

A full-bridge inverter with bipolar PWM operating in CCM has been regarded as the best configuration from the leakage current suppression perspective because V_{cm} is always kept constant as $V_{\mathrm{DC}}/2$. This system achieves a completely symmetrical structure, such that the high frequency noise source at each phase leg, mostly dv/dt at the switching node, cancels each other [24]. In this section, the impact of CRM operation on the CM voltage, and how the high frequency leakage current is generated, are explored in depth.

Fig. 7(a) and (b) shows the switching cycle waveforms of the CRM full-bridge inverter and CCM full-bridge inverter in bipolar mode without (solid line) and with (dotted line) the line frequency leakage current for the positive half line cycle, respectively. It should be noted that the first resonant period (Stage II) described in Section II is assumed to be very short and negligible compared to the second resonant period (Stage IV), and is not considered for the leakage current analysis in Fig. 7. As for the CRM case, without the line frequency leakage current, the CM voltage remains constant as $V_{\mathrm{DC}}/2$ since V_{aN} and V_{bN} change at the same rate during the resonant period, t_3–t_4, which only exists in CRM operation assuming Q_1/Q_4 and Q_2/Q_3 are switching complementarily. With the line frequency leakage current, though the element is very small, it brings a notable implication on the system. The small difference of i_{L1} and i_{L2} expressed as i_{Lk_L1} and i_{Lk_L2} due to the line frequency leakage current i_{Lk_L} brings about the zero-crossing timing mismatch for the inductor currents. Then, the resonance starting points of switching nodes V_{aN} and V_{bN} become inconsistent with each other such that a bump appears in V_{cm}; this is marked as the green shaded area in Fig. 7(a). The CM voltage is no longer constant. Eventually, the nonconstant V_{cm} becomes the source of the high frequency leakage current in the system. Due to the inherent operating status in CRM, the resonant period, the CM voltage variation occurs. This phenomenon is not important in CCM operation as shown in Fig. 7(b), because SRs are conducted reversely (interval t_3–t_4) before the active switches are turned ON, and there is no such resonant period. It is clearly seen that there is no bump in the CCM case, even though the line frequency leakage current exists. Basically, the penalty of using

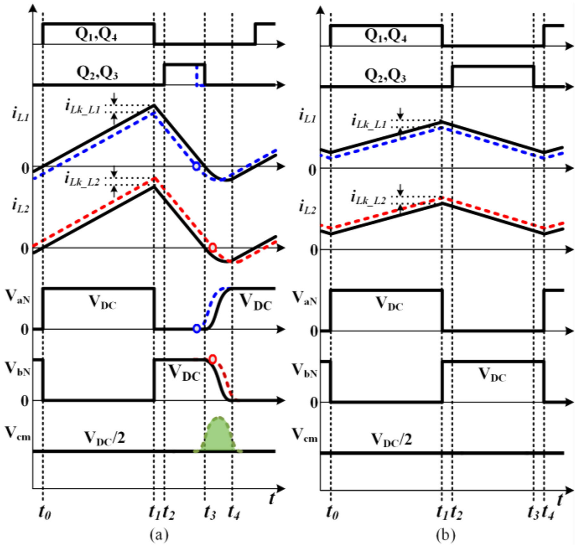

Fig. 7. Switching cycle waveforms of (a) CRM full-bridge inverter in bipolar mode and (b) CCM full-bridge inverter in bipolar mode without (solid line) and with (dotted line) the line frequency leakage current. The green shaded area in $\mathrm{V_{cm}}$ represents nonconstant part that becomes a source of the high frequency leakage current in (a).

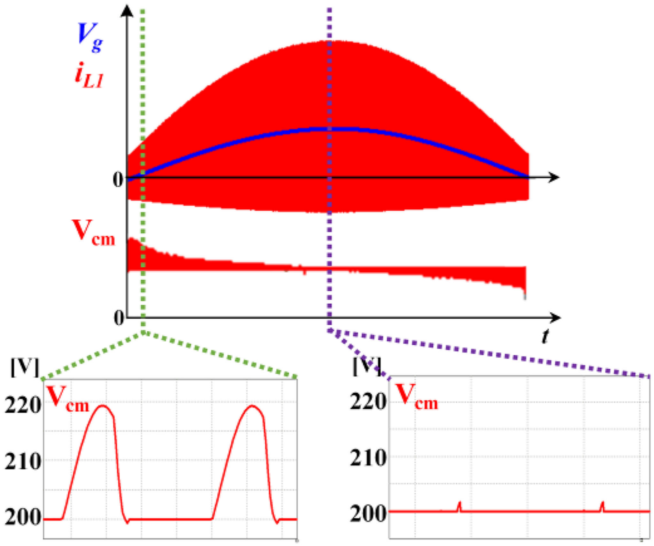

Fig. 8. CM voltage comparison at the peak of ac voltage and near zero crossing of ac voltage.

CRM to achieve ZVS for high efficiency and high power density is the additional CM noise source causing larger leakage current. Please note that the figure depicts the switching cycle at which the line frequency leakage current is negative. When the line frequency leakage current is positive, the bump in V_{cm} appears in the opposite direction.

The variation of the CM voltage is dependent on the magnitude of the line frequency leakage current and the switching frequency of the inverter. For instance, the zero-crossing mismatch of the two inductors becomes more severe with a larger line frequency leakage current. In addition, the resonant period takes up a greater proportion of one switching cycle if switching frequency is high [10]. As shown in Fig. 5, the line frequency leakage current is the largest at the ac voltage zero crossing. Besides, the switching frequency of the inverter in CRM also becomes higher as the ac voltage approaches zero crossing due to small inductor current. Thus, it is expected that, near the ac voltage zero crossing, the bump in V_{cm} is much larger and longer than the ac voltage peak area.

Fig. 8 compares the CM voltage at the peak and near the zero crossing of the ac voltage. It clearly shows that V_{cm} becomes more severe near the ac voltage zero crossing as compared with the ac voltage peak area producing more high frequency leakage current. Thus, careful attention needs to be paid near the ac voltage zero crossing to control the high frequency leakage current.

IV. PROPOSED SWITCHING MODULATION STRATEGIES FOR LEAKAGE CURRENT SUPPRESSION

When the dc-ac inverter operates in CRM, the switching frequency varies over the line cycle, as shown by the blue line in Fig. 9(a). This is based on the accurate mathematical model for the switching frequency of ac-dc converters in CRM introduced in [11]. The wide variation of the switching frequency is not desirable because of a burden upon control and increased switching loss. One simple way to shrink the frequency range is to use discontinuous conduction mode (DCM) near the ac voltage zero crossing [12]. Fig. 9 depicts the switching frequency distribution of the CRM full-bridge inverter in bipolar mode, and how to limit the switching frequency with DCM. Here, when the frequency is higher than a specific level, 1 MHz (red shaded area), turn-ON for the active switches is delayed, such that the inductor current resonates after the inductor current comes back to zero from negative value. The delay continues until one resonant cycle ends as illustrated in Fig. 9(b) representing Region I in Fig. 9(a) and is expressed in terms of the inductor and the output capacitance of the power devices

$$T_{\mathrm{delay,regionI}} = \frac{2\pi}{\omega_0} = 2\pi\sqrt{LC_{\mathrm{oss}}}. \tag{9}$$

If the switching frequency exceeds the limit even with the resonant cycle delay, another resonant cycle delay is added as shown in Fig. 9(c) [Region II in Fig. 9(a)] given as

$$T_{\mathrm{delay,regionII}} = 2\cdot\frac{2\pi}{\omega_0} = 4\pi\sqrt{LC_{\mathrm{oss}}}. \tag{10}$$

With this method, the switching frequency of the inverter can be clamped and plotted as the red line in Fig. 9(a). However, it can be inferred that introducing DCM near zero crossing gives rise to larger high frequency leakage current as the elongated resonant time worsens V_{cm}, as shown in Fig. 9(b) and (c).

A. *Approach I: CRM + Triangular Current Mode*

In order to avoid the lengthened resonant time with DCM, triangular current mode (TCM) is adopted near the ac voltage

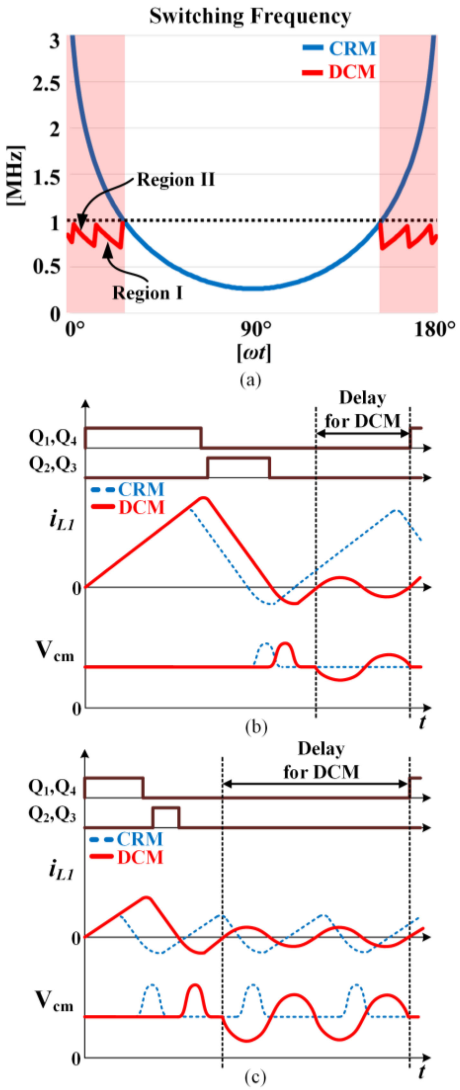

(a)

(b)

(c)

Fig. 9. Clamping maximum switching frequency with DCM. (a) Switching frequency distribution (blue line: CRM, red line: DCM). (b) Waveforms of Q_1–Q_4 for DCM, i_{L1} and $V_{\rm cm}$ for CRM (blue dotted line) and DCM (red line) in Region I. (c) Waveforms of Q_1–Q_4 for DCM, i_{L1} and $V_{\rm cm}$ for CRM (blue dotted line) and DCM (red line) in Region II.

zero crossing instead of DCM. When the switching frequency is higher than the maximum frequency limit, the OFF-time of the active switches is extended by turning ON the SRs for a longer period of time, so called OFF-time extension. By using OFF-time extension, the inductor current becomes a triangle-like shape and has a larger negative inductor current. The resonant period can be shortened by means of larger energy stored in the inductor. Thus, variation of $V_{\rm cm}$ is minimized as shown in Fig. 10(b) compared to that in CRM. Originally, TCM is employed to achieve ZVS when energy stored in the inductor is not enough to discharge the output capacitors of the active switches [8], yet here it is used for the high frequency leakage current reduction. By combining CRM and TCM, the full-bridge inverter with bipolar PWM can always achieve ZVS and suppress the leakage current with a narrow switching frequency range.

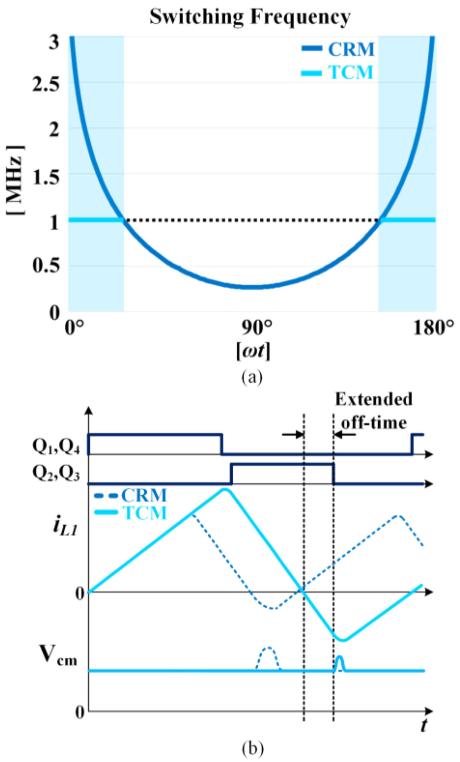

(a)

(b)

Fig. 10. Clamping maximum switching frequency with TCM. (a) Switching frequency distribution in half line cycle (blue line: CRM, light blue line: TCM). (b) Waveforms of Q_1–Q_4 for TCM, i_{L1} and $V_{\rm cm}$ for CRM (blue dotted line) and TCM (light blue line).

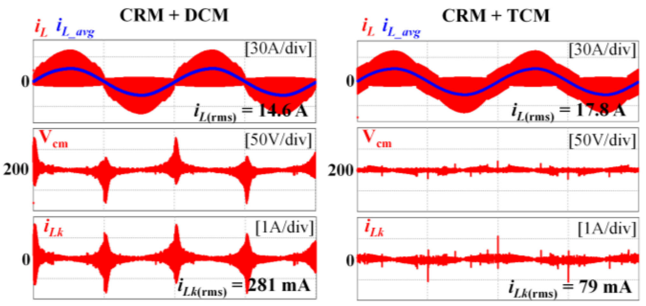

(a)

(b)

Fig. 11. Line cycle simulation waveforms comparison. (a) CRM + DCM. (b) CRM + TCM.

Fig. 11 shows simulation results comparing CRM + DCM and CRM + TCM cases for two-line cycles under full load condition. The system specification is organized in Section V. It is observed that the CRM + TCM method has much smaller $V_{\rm cm}$ near the ac voltage zero crossing resulting in a significant reduction in the rms value of the leakage current. However, the rms value of the inductor current rises substantially due to the enlarged negative current by the OFF-time extension. This definitely causes extra losses, especially conduction loss and turn-OFF loss of the GaN devices; thus, efficiency is reduced. (The turn-OFF loss is minor due to the minute turn-OFF energy of GaN devices; therefore, the conduction loss will be sorely considered in the following

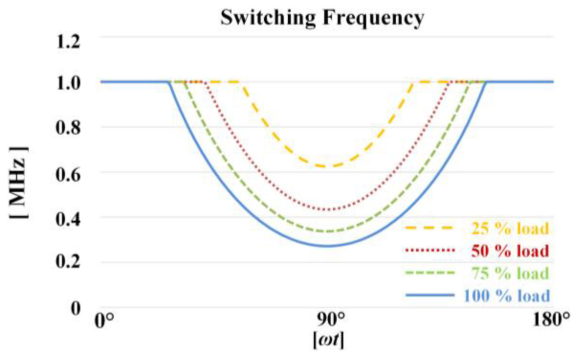

Fig. 12. Switching frequency distribution with CRM + TCM under different load conditions.

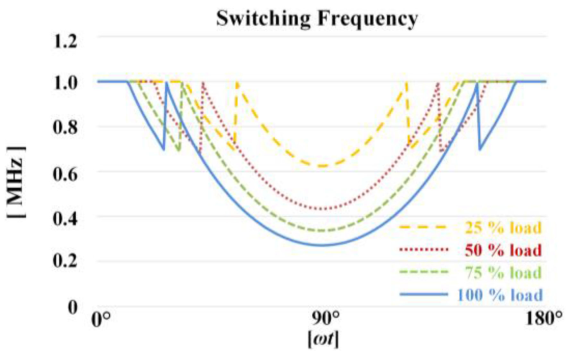

Fig. 14. Switching frequency distribution with CRM + DCM + TCM under different load conditions.

discussion.) Assuming that the maximum clamping frequency is always fixed at 1 MHz regardless of load conditions, it is anticipated that the conduction loss by the large current ripple soars under the light load condition since the TCM operation accounts for a higher portion compared with the heavy load condition, as shown in Fig. 12. In [28], the measured efficiency of the inverter with the CRM + TCM method drops rapidly as the output power decreases. For the PV inverter, the light load efficiency is as important as the heavy load efficiency because of a term called "weighted efficiency" that takes into account the light load efficiency in accordance with the inverter operating profile for a day.

B. Approach II: CRM + DCM + TCM

Furthering [28], a new modulation strategy is proposed to compensate for the disadvantage of Approach I. Based on observation of the simulation results in Fig. 11, there is still sufficient margin to the leakage current requirement when the CRM full-bridge inverter runs in combination with TCM. Therefore, the leakage current is slightly sacrificed in order to reduce the large inductor current ripple. This can be done by adding the DCM operation into Approach I. The key idea of the new approach is a tradeoff between the leakage current and the efficiency.

The DCM operation is inserted between CRM and TCM as represented in Fig. 13. The reason why DCM is not placed next to the ac voltage zero crossing is to avoid extreme V_{cm} and larger leakage current. As shown in Figs. 9(c) and 11(a), V_{cm} deteriorates dramatically as the ac voltage draws near the zero crossing because more than one resonant cycle delay is given for the DCM operation. It is possible to widen the DCM operation area, but a price would be paid in terms of an increase in the leakage current. Thus, here, DCM is introduced in a small area where only one resonant cycle delay is given, as depicted in Fig. 9(b). As a result, the switching frequency distribution over the line cycle becomes as shown in Fig. 14 under the different load conditions.

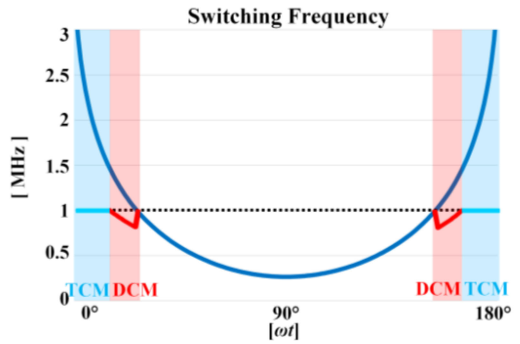

Fig. 13. Switching frequency distribution with CRM + DCM + TCM modulation (blue line: CRM, red line: DCM, light blue line: TCM).

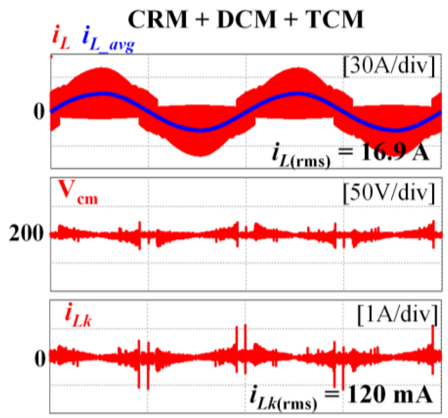

Fig. 15. Line cycle simulation waveforms with CRM + DCM + TCM.

Fig. 15 shows the simulation waveforms of the proposed method under full load condition. In comparison with Fig. 11 (b), it is noticed that V_{cm} in this case deteriorates due to the lengthened resonant period for the DCM operation; that gives rise to larger leakage current. Although the leakage current increases by 41 mA, there is still enough margin to the required value, and the rms value of the inductor current decreases by 0.9 A, which helps to improve efficiency.

It should be noted that in Figs. 10(a) and 13, the switching frequency in the blue shaded area, the TCM region, is fixed as constant value. It is possible to further lower the maximum switching frequency to reduce switching loss, but the inductor current ripple increases, causing even larger conduction loss in such a case. Switching loss and conduction loss can also be another tradeoff for designing the inverter. Furthermore, the maximum switching frequency does not have to be constant with TCM. For example, it can linearly increase or decrease as being close to the zero crossing. There are diverse options to select the maximum switching frequency; however, since it is not the main focus of this work, it will be left open. In summary, by combining CRM and TCM, a full-bridge inverter with bipolar PWM can effectively suppress the leakage current with a narrow switching frequency range. Introducing DCM in a small region between CRM and TCM can supplement efficiency with reduced conduction loss.

C. Control Structure of the Proposed Method

Fig. 16(a) represents the overall control structure of the proposed switching modulation method, particularly Approach II. The input voltage V_{DC}, the ac voltage V_g, and the inductor current i_L are sensed, and zero crossing of the inductor current is detected (ZCD) in order to control the inverter. The inductor current is averaged by a low pass filter and controlled to track the output ac current reference i_{L_ref}. The average current compensator outputs the control signal v_c which denotes ON-time for CRM and DCM and duty cycle for TCM [8]. This value is employed to generate PWM signals.

First, the operation mode of the inverter is pre-determined with look-up tables. With given input voltage, ac voltage and load conditions, the switching frequency distribution and the operation mode shown in Fig. 14 can be obtained. According to the phase angle information, θ_g, of the ac voltage from the phase locked loop (PLL) function, the operation mode is selected over the line cycle. It is worth noting that the calculation of the switching frequency can be executed online and so can the operation mode selection, but it requires high calculation capability of microcontrollers due to the high calculation burden.

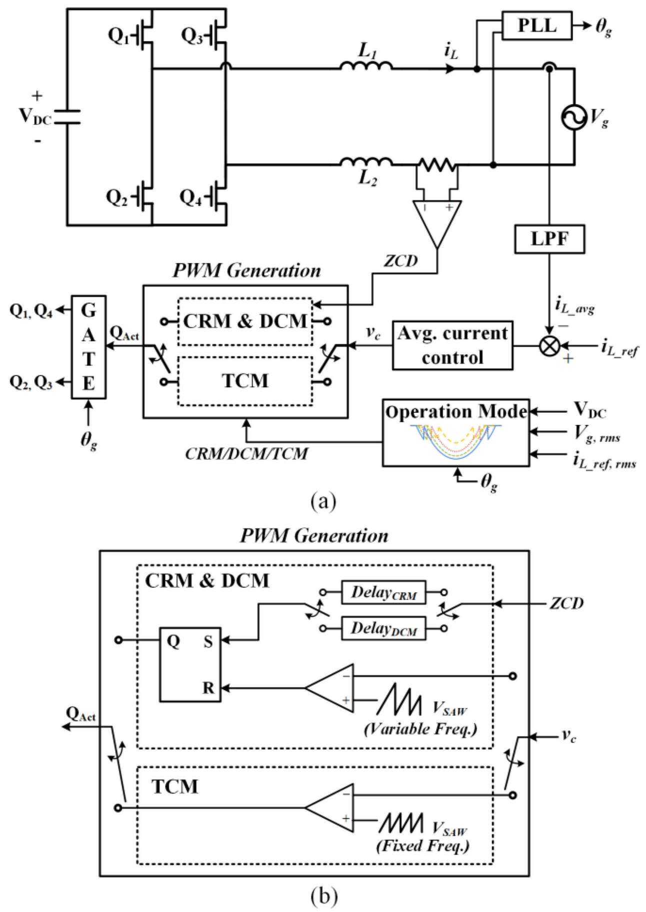

(a)

(b)

Fig. 16. Control structure of the proposed modulation method. (a) Overall. (b) Details of PWM generation for CRM/DCM/TCM mode.

With the operation mode selected at a certain moment, the control signal v_c is processed in different ways, as shown in Fig. 16(b). For example, for CRM and DCM, the ZCD signal is necessary for the variable switching frequency. The ZCD signal acts as the trigger of each switching cycle. Once the zero-crossing of the inductor current is detected, some delay is given before the active switches are turned ON. The delay for CRM is the resonant period during Stage IV to achieve ZVS derived from (4) as follows:

$$\text{Delay}_{\text{CRM}} = \frac{\pi - \arccos\left(\frac{V_{DC}-V_g}{V_{DC}+V_g}\right)}{\omega_0}. \tag{11}$$

The delay for DCM consists of the time intervals in Stages IV and V as well as one resonant cycle in (9) to ensure soft-switching given as

$$\begin{aligned}\text{Delay}_{\text{DCM}} &= \frac{\pi - \arccos(\frac{V_{DC}-V_g}{V_{DC}+V_g})}{\omega_0} + \frac{L}{2Z_0}\cdot\frac{V_{DC}-V_g}{V_{DC}+V_g} + \frac{2\pi}{\omega_0}\\ &= \frac{1}{\omega_0}(3\pi - \arccos\left(\frac{V_{DC}-V_g}{V_{DC}+V_g}\right) + \frac{V_{DC}-V_g}{V_{DC}+V_g}).\end{aligned} \tag{12}$$

Then, the turn-OFF instant of the active switches is decided by comparing the control signal with the carrier signal V_{SAW}, which is synchronized with the ZCD signal. Note that the delays for the CRM and DCM operations can be calculated either offline or online. When it comes to the SRs, the turn-ON instant is decided based on the required deadtime. Then, the SRs are turned OFF when the ZCD signal becomes active.

With regard to the TCM operation, there is no need for the ZCD signal due to its fixed switching frequency. The turn-ON of the active switches is triggered by the fixed frequency carrier signal and the turn-OFF instant is determined by the control signal. The SRs are complementarily turned ON and OFF in accordance with the active switches with the deadtime.

V. EXPERIMENTAL RESULTS

A prototype of the single-phase transformerless full-bridge inverter with the proposed switching modulation strategy is implemented to validate the performance of the inverter. The specification of the prototype is organized in Table I. The stray capacitance is chosen for the worst scenario described in [26] where the capacitance increases 100 to 160 nF per kW power due to water on the PV panel.

The photograph of the prototype is shown in Fig. 17. The hardware consists of GaN devices, driving circuits, input capacitors, output inductors, an additional output LC filter, and sensing circuits. The GaN devices are attached right on the top layer of

TABLE I
SPECIFICATION OF THE PROTOTYPE

Condition	Value
Maximum Load Power (P_o)	2.4 kW
Input Voltage (V_{DC})	400 V
Output AC Voltage (V_g)	220 Vrms/60 Hz
Output Inductor (L_1, L_2)	3.5 µH
Switching Frequency (F_s)	300 kHz – 1 MHz
Stray Capacitance (C_{PV})	300 nF
GaN device (Q_1, Q_2, Q_3, Q_4)	GS66516T (650V, 60A)

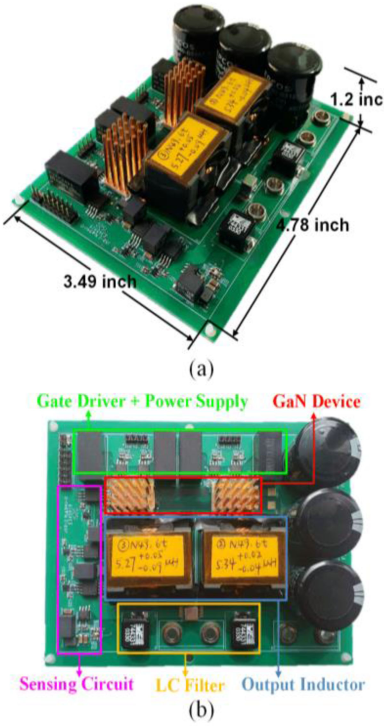

(a)

(b)

Fig. 17. Laboratory prototype of 2.4-kW full-bridge inverter. (a) Overall view. (b) Top view.

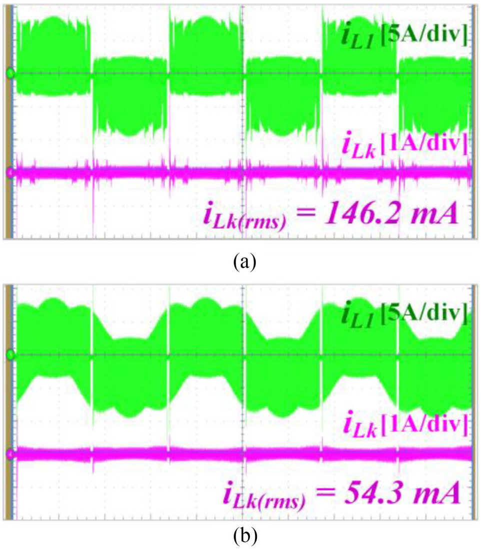

(a)

(b)

Fig. 18. Leakage current comparison. (a) CRM + DCM. (b) CRM +TCM. Both cases under $V_{\mathrm{DC}} = 200$ V, $V_g = 110$ V, and $P_o = 250$ W.

the circuit board and the heat sinks are attached above the GaN devices. It should be mentioned that the maximum current rating for the GaN devices needs to be higher than that of CCM PV inverter due to the large inductor current ripple. For the gate driving circuit, SI8271GB is used to drive the GaN device and powered by an isolated dc-dc power supply, MEJ1S0505. The additional output LC filter is designed to attenuate output current ripple in the way that total harmonic distortion (THD) at full load is lower than 3% for the CRM + TCM case. The cutoff frequency of the LC filter is approximately 88 kHz (inductor: 3.3 μH for each, capacitor: 0.5 μF). It can be seen that the additional LC filter takes up only a small space of the hardware by means of its high cutoff frequency. A microcontroller, TMS320F28379D, is externally connected to the prototype to process the sensing information and generate PWM signals. Eventually, the power density of the prototype is 151 W/inch^3 (9.25 kW/L) excluding the input capacitors.

Fig. 18 compares the leakage current of the two switching modulation methods (CRM + DCM versus CRM + TCM) at the same operating condition ($V_{\mathrm{DC}} = 200$ V, $V_g = 110$ V, and $P_o = 250$ W). The rms value of the leakage current in the first case is 146.2 mA, and the other case has 54.3 mA. As expected, the CRM + DCM operation results in much larger leakage current, and the CRM + TCM operation features better performance for the leakage current.

Fig. 19 illustrates the ac voltage V_g, the output current i_g, L_1 inductor current i_{L1}, and the leakage current i_{Lk}, under half load (1.2-kW) and full load (2.4-kW) conditions. It is shown that the output current is sinusoidal and in phase with the ac voltage. Moreover, the leakage current near zero crossing is well suppressed. However, at the half load condition, a portion of TCM is much higher than the full load condition, which brings about an adverse impact on conduction loss with the large inductor current ripple.

Waveforms in Fig. 20 represent the same as those in Fig. 18, except that the inverter is operated with the proposed CRM + DCM + TCM modulation scheme. One notable difference is a significant reduction in the inductor current ripple due to a smaller portion of the TCM operation. At the same time, the leakage current increases at the cost of the smaller inductor current ripple. It is noteworthy that the rms current reduction effect is quite obvious for the lower load condition, which certainly benefits light load efficiency improvement.

Also, it is worth noting that, on the basis of observing the leakage current in Figs. 19 and 20, it appears that large turn-OFF current at heavy load has dominant impacts on the leakage current near the ac voltage peak area instead of the CM voltage caused by the resonant period near zero crossing. This is not covered in this study and left for future work.

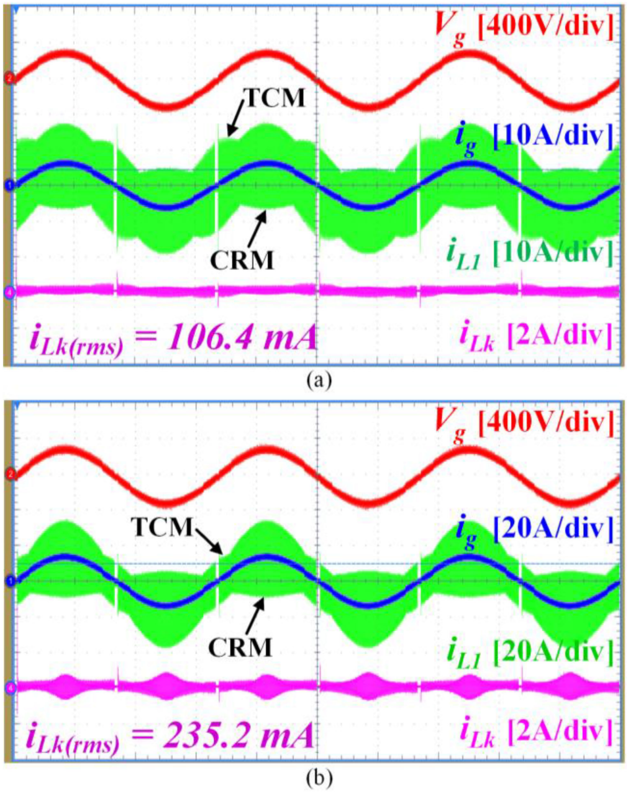

Fig. 19. Experimental waveforms of full-bridge inverter with bipolar PWM operating at CRM combined with TCM. (a) Under 1.2-kW load condition. (b) Under 2.4-kW load condition.

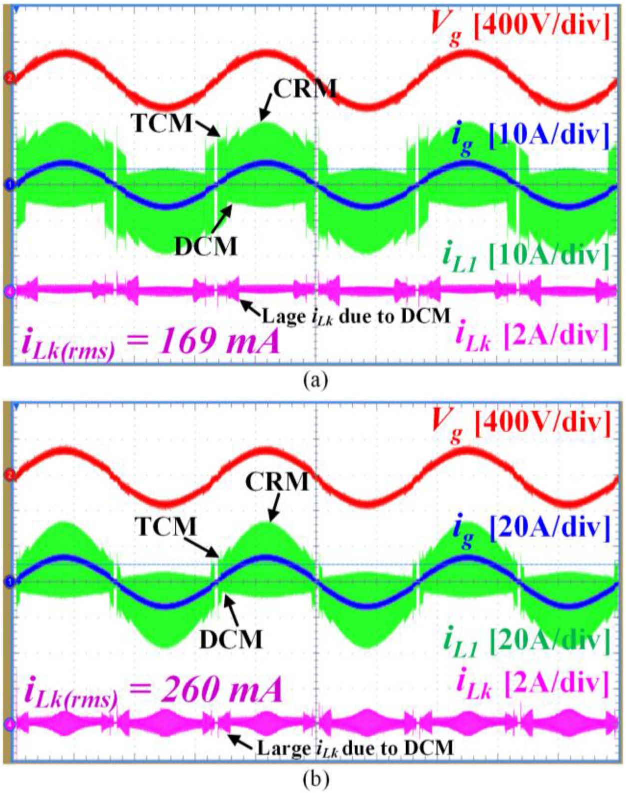

Fig. 20. Experimental waveforms of full-bridge inverter with bipolar PWM operating at CRM combined with DCM and TCM. (a) Under 1.2-kW load condition. (b) Under 2.4-kW load condition.

Fig. 21 shows the Q_1 gate-to-source signal V_{GS1}, L_1 inductor current i_{L1}, output current i_g, and Q_1 drain-to-source voltage V_{DS1} under the 2.4-kW load condition with the CRM + DCM + TCM operation. In Fig. 21, the zoomed waveforms (left: TCM operation, middle: DCM operation, right: CRM operation) delineate the switching cycle behavior of the inverter showing that the active switch is always turned ON after the drain-to-source voltage of the active switch reaches zero in both CRM and TCM operations. These results match with the analysis of the operation principle in Section II. In the TCM operation region, ZVS is always guaranteed since even more energy is stored in the inductor compared with the CRM operation. An interesting point is that ZVS can be also achieved in most of the DCM operation regions. Since one resonant cycle delay is given, as shown in Fig. 9(b), the inductor current at the active switch turn-ON instant is mostly zero. The corresponding drain-to-source voltage at this instant is zero. Based on the results from the experiment, more than 95% of the DCM operation region can fulfill ZVS. Although some turn-ON loss is generated by the non-ZVS area, it is minute.

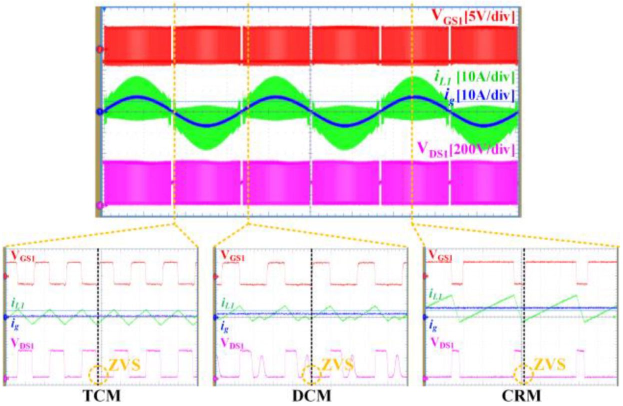

Fig. 21. Measured gate-to-source voltage of Q_1, L_1 inductor current, output current, and drain-to-source voltage of Q_1 under full-load condition (left: TCM, middle: DCM, right: CRM).

The measured efficiency of the inverter and the leakage current for both approaches under different load conditions are plotted in Fig. 22. With the CRM + TCM method, the rms value of the leakage current is suppressed below 300 mA under various load conditions. The peak efficiency of the inverter is slightly higher than 98% around 80% load condition. However, efficiency drops rapidly as the output power becomes lower as expected. This is because of the increased portion of the TCM operation leading to larger conduction loss. By combining DCM and TCM with CRM, efficiency is improved, especially at light load, by 0.1 to 1.1%. At this time, the peak efficiency becomes 98.1%. Meanwhile, the leakage current increases; however, it still remains below 300 mA without an additional filter at the output side.

Fig. 23 compares measured THD of the output current. When the output power is high (above 60% load), THD of the CRM + TCM case is larger than that of the CRM + DCM + TCM

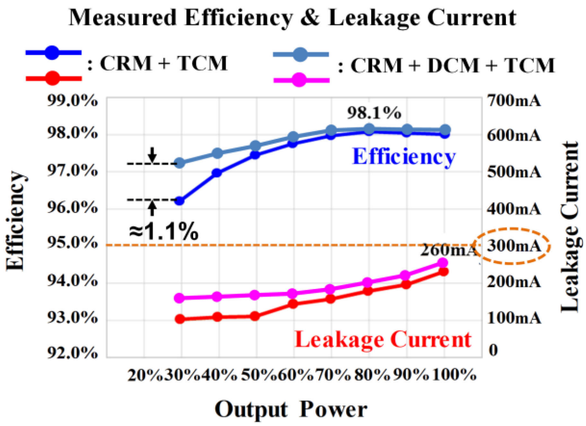

Fig. 22. Measured efficiency and leakage current under different load conditions with both CRM + TCM and CRM + DCM + TCM methods.

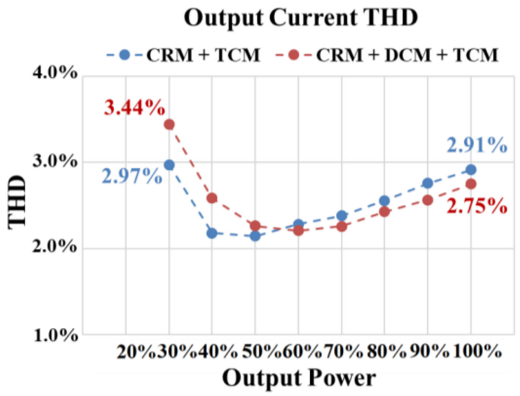

Fig. 23. Measured THD of output current under different load conditions with both CRM + TCM and CRM + DCM + TCM methods.

case because of the larger current ripple at the output current. However, interestingly, when the output power is low (below 50% load), the result is totally opposite. The main reason is that the impact of the mode transition becomes more noticeable. This mode transition causes small ringing in the output current. The ringing has more impact on THD than the inductor current ripple at light load. Since Approach II (CRM + DCM + TCM) has one more mode transition compared to Approach I (CRM + TCM), THD of the former method becomes slightly larger at light load although the inductor current ripple is much smaller than that of the latter method. The efficiency data in Fig. 22 and THD data in Fig. 23 are collected by a PZ-4000 power analyzer.

VI. CONCLUSION

In this article, a CRM single-phase transformerless PV inverter for residential systems is explored. Regardless of operation conditions, the CRM full-bridge in bipolar mode always achieves ZVS, which enables high frequency operation. However, the small current difference in the two output inductors caused by the line frequency leakage current leads to nonconstant CM voltage during the resonant period, and forms the high frequency leakage current. In order to suppress the leakage current, TCM operation is introduced near the ac voltage zero crossing. The resonant period becomes shorter, and the CM voltage is soothed. For the purpose of improving efficiency, DCM is inserted in between CRM and TCM, sacrificing the leakage current slightly. The experimental results verify the leakage current suppression performance of the inverter with both modulation methods. By virtue of the CRM operation with GaN devices, switching frequency is pushed above 300 kHz, and 151 W/in^3 power density is achieved.

REFERENCES

[1] J. M. A. Myrzik and M. Calais, “String and module integrated inverters for single-phase grid connected photovoltaic systems—A review,” in *Proc. IEEE Bologna Power Tech. Conf. Proc.*, Bologna, Italy, 2003, vol. 2, Art. no. 8.

[2] R. Gonzalez, J. Lopez, P. Sanchis, and L. Marroyo, “Transformerless inverter for single-phase photovoltaic systems,” *IEEE Trans. Power Electron.*, vol. 22, no. 2, pp. 693–697, Mar. 2007.

[3] S. V. Araujo, P. Zacharias, and R. Mallwitz, “Highly efficient single-phase transformerless inverters for grid-connected photovoltaic systems,” *IEEE Trans. Ind. Electron.*, vol. 57, no. 9, pp. 3118–3128, Sep. 2010.

[4] W. Zhang, X. Huang, F. C. Lee, and Q. Li, “Gate drive design considerations for high voltage cascode GaN HEMT,” *in Proc. IEEE Appl. Power Electron. Conf. Expo.-APEC 2014*, Fort Worth, TX, USA, 2014, pp. 1484–1489.

[5] X. Huang, Z. Liu, F. C. Lee, and Q. Li, “Characterization and enhancement of high-voltage cascode GaN devices,” *IEEE Trans. Electron. Devices*, vol. 62, no. 2, pp. 270–277, Feb. 2015.

[6] X. Huang, Z. Liu, Q. Li, and F. C. Lee, “Evaluation and application of 600 V GaN HEMT in cascode structure,” *IEEE Trans. Power Electron.*, vol. 29, no. 5, pp. 2453–2461, May 2014.

[7] C. Sørensen *et al.*, “Conduction, reverse conduction and switching characteristics of GaN E-HEMT,” in *Proc. IEEE 6th Int. Symp. Power Electron. Distrib. Gener. Syst. (PEDG),* Aachen, Germany, 2015, pp. 1–7.

[8] Z. Liu, B. Li, F. C. Lee, and Q. Li, “High-efficiency high-density critical mode rectifier/inverter for WBG-Device-Based on-board charger,” *IEEE Trans. Ind. Electron.*, vol. 64, no. 11, pp. 9114–9123, Nov. 2017.

[9] Z. Liu, Z. Huang, F. C. Lee, and Q. Li, “Digital-based interleaving control for GaN-based MHz CRM totem-pole PFC,” *IEEE J. Emerg. Sel. Topics Power Electron.*, vol. 4, no. 3, pp. 808–814, Sep. 2016.

[10] Z. Liu, F. C. Lee, Q. Li, and Y. Yang, “Design of GaN-based MHz totem-pole PFC rectifier,” *IEEE J. Emerg. Sel. Topics Power Electron.*, vol. 4, no. 3, pp. 799–807, Sep. 2016.

[11] Y. Yang, Z. Liu, F. C. Lee, and Q. Li, “Analysis and filter design of differential mode EMI noise for GaN-based interleaved MHz critical mode PFC converter,” in *Proc. IEEE Energy Convers. Congr. Expo. (ECCE)*, Pittsburgh, PA, USA, 2014, pp. 4784–4789.

[12] Z. Liu, “Characterization and application of wide-band-gap devices for high frequency power conversion,” Ph.D. dissertation, Dept. ECE, Virginia Tech, Blacksburg, VA, USA, 2017.

[13] C. Marxgut, F. Krismer, D. Bortis, and J. W. Kolar, “Ultraflat interleaved triangular current mode (TCM) single-phase PFC rectifier,” *IEEE Trans. Power Electron.*, vol. 29, no. 2, pp. 873–882, Feb. 2014.

[14] *Automatic disconnection device between a generator and the public low-voltage grid*, DIN VDE 0126-1-1, 1999.

[15] R. Gonzalez, J. Lopez, P. Sanchis, and L. Marroyo, “Transformerless inverter for single-phase photovoltaic systems,” *IEEE Trans. Power Electron.*, vol. 22, no. 2, pp. 693–697, Mar. 2007.

[16] M. Victor, F. Greizer, S. Bremicker, and U. Hübler, “Method of converting a direct current voltage from a source of direct current voltage, more specifically from a photovoltaic source of direct current voltage, into an alternating current voltage,” U.S. Patent 7 411 802, Aug. 12, 2008.

[17] L. Zhang, K. Sun, Y. Xing, and M. Xing, “H6 transformerless full-bridge PV grid-tied inverters,” *IEEE Trans. Power Electron.*, vol. 29, no. 3, pp. 1229–1238, Mar. 2014.

[18] E. Akpınar, A. Balıkcı, E. Durbaba, and B. T. Azizoğlu, “Single-phase transformerless photovoltaic inverter with suppressing resonance in improved H6,” *IEEE Trans. Power Electron.*, vol. 34, no. 9, pp. 8304–8316, Sep. 2019.

[19] H. Li, Y. Zeng, B. Zhang, T. Q. Zheng, R. Hao, and Z. Yang, “An improved H5 topology with low common-mode current for transformerless PV grid-connected inverter,” *IEEE Trans. Power Electron.*, vol. 34, no. 2, pp. 1254–1265, Feb. 2019.

[20] H. Xiao, S. Xie, Y. Chen, and R. Huang, “An optimized transformerless photovoltaic grid-connected inverter,” *IEEE Trans. Ind. Electron.*, vol. 58, no. 5, pp. 1887–1895, May 2011.

[21] S. Heribert, S. Christoph, and K. Jurgen, “Inverter for transforming a DC voltage into an AC current or an AC voltage,” Europe Patent 1 369 985 (A2), May 13, 2003.

[22] H. F. Xiao, K. Lan, and L. Zhang, “A quasi-unipolar SPWM full-bridge transformerless PV grid-connected inverter with constant common-mode voltage,” *IEEE Trans. Power Electron.*, vol. 30, no. 6, pp. 3122–3132, Jun. 2015.

[23] W. Li, Y. Gu, H. Luo, W. Cui, X. He, and C. Xia, “Topology review and derivation methodology of single-phase transformerless photovoltaic inverters for leakage current suppression,” *IEEE Trans. Ind. Electron.*, vol. 62, no. 7, pp. 4537–4551, Jul. 2015.

[24] M. Shoyama, G. Li, and T. Ninomiya, “Balanced switching converter to reduce common-mode conducted noise,” *IEEE Trans. Ind. Electron.*, vol. 50, no. 6, pp. 1095–1099, Dec. 2003.

[25] L. Ma, F. Tang, F. Zhou, X. Jin, and Y. Tong, “Leakage current analysis of a single-phase transformer-less PV inverter connected to the grid,” in *Proc. IEEE Int. Conf. Sustain. Energy Technol.,* Singapore, 2008, pp. 285–289.

[26] “Capacitive leakage currents,” SMA Technical Information, AbleitstromTI-en-25, version 2.5.

[27] E.Gubía, P.S., A.Ursúa, J. L., and L. Marroyo, “Ground currents in single-phase transformerless photovoltaic systems,” *Prog. Photovolt., Res. Appl.*, vol. 15, no. 7, pp. 629–650, 2007.

[28] G. Son, Z. Huang, Q. Li, and F. C. Lee, “Critical conduction mode based high frequency single-phase transformerless PV inverter,” in *Proc. IEEE Appl. Power Electron. Conf. Expo. (APEC)*, New Orleans, LA, USA, 2020, pp. 3232–3237.

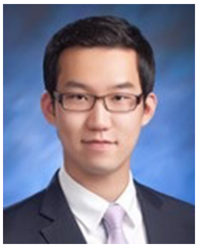

Gibong Son (Student Member, IEEE) received the B.S. degree in electrical engineering from Pusan National University, Pusan, South Korea, in 2012, and the M.S. degree in electrical engineering from Seoul National University, Seoul, South Korea, in 2014. He has been working toward the Ph.D. degree with Virginia Polytechnic Institute and State University, Blacksburg, VA, USA, since 2018.

He was with Hyundai Motor Company from 2014 to 2018 developing power-conversion system in electric vehicles. His research interests include high-frequency soft-switching ac/dc converters, resonant converters, and power conversion in automotive and renewable energy applications.

Zhengrong Huang (Student Member, IEEE) received the B.S. degree in electrical engineering from Tsinghua University, Beijing, China, in 2014, and the Ph.D. degree in electrical engineering from Virginia Polytechnic Institute and State University, Blacksburg, VA, USA, in 2020.

He is currently with Analog Devices Inc., Santa Clara, CA, USA. His research interests include high-frequency ac/dc power conversion with soft-switching techniques, applications of wide bandgap power semiconductor devices, and digital control.

Qiang Li (Member, IEEE) received the B.S. and M.S. degrees in power electronics from Zhejiang University, Hangzhou, China, in 2003 and 2006, respectively, and the Ph.D. degree in electrical engineering from Virginia Polytechnic Institute and State University, Blacksburg, VA, USA, in 2011.

He is currently an Associate Professor with the Center for Power Electronics Systems, Virginia Polytechnic Institute and State University. His research interests include power management for distributed power systems, applications of wide-bandgap power devices, high-frequency power conversion and controls, magnetics and EMI, high-density electronics packaging and integration, and renewable energy.

Dr. Li is the recipient of the First Place Prize Paper Award for 2016 in the IEEE TRANSACTIONS ON POWER ELECTRONICS. He is also a recipient of the 2017 National Science Foundation (NSF) Career Award.

Fred C. Lee (Fellow, IEEE) received the B.S. degree in electrical engineering from the National Cheng Kung University, Tainan City, Taiwan, in 1968, and the M.S. and Ph.D. degrees in electrical engineering from Duke University, Durham, NC, USA, in 1972 and 1974, respectively.

He is currently a University Distinguished Professor Emeritus with Virginia Polytechnic Institute and State University (Virginia Tech), Blacksburg, VA, USA, and the Founder and Director Emeritus of the Center for Power Electronics Systems, an engineering research center consisting of 80 corporations. The mission of the center is “to provide leadership through global collaboration to create electric power processing systems of the highest value to society.” He holds 94 U.S. patents, and has authored/coauthored more than 310 journal articles and more than 740 refereed technical papers. During his tenure at Virginia Tech, he has supervised to completion 87 Ph.D. and 93 Master’s students. His research interests include high-frequency power conversion, magnetics and EMI, distributed power systems, renewable energy, power quality, high-density electronics packaging and integration, and modeling and control.

Dr. Lee was the President of the IEEE Power Electronics Society from 1992 to 1994 and is a recipient of the William E. Newell Power Electronics Award in 1989; PCIM Award for Leadership in Power Electronics Education presented at HFPC in 1990; the Arthur E. Fury Award for Leadership and Innovation in1998; the Honorary Sun Yuen Chuan Chair Professor of National Tsing Hua University in Taiwan in 2001; the Ernst-Blickle Award sponsored by SEW-EURODRIVE Foundation in 2005; the Distinguished Alumni Award from National Cheng Kung University in 2006; the Honorary Li Kwoh-Ting Chair Professor of National Cheng Kung University in 2011; Life Fellow of IEEE and inaugural member of the Virginia Tech Entrepreneur Hall of Fame in 2012; Honorary Chair Professor of National Chiao Tung University in Taiwan in 2014; Honorary Chair Professor of Tsinghua University in China in 2017; and Honorary Professor of Huazhong University of Science and Technology in China in 2018. He is a member of the U.S. National Academy of Engineering, an Academician of the Academia Sinica in Taiwan, and a foreign member of the Chinese Academy of Engineering in the People.s Republic of China. He is a recipient of the IEEE Medal in Power Engineering in 2015 "for contributions to power electronics, especially highfrequency power conversion," the Power Supply Technology Outstanding Achievement Award from China Power Supply Society in 2017, and was elected as a National Academy of Inventors Fellow in 2018.